Earth and Planetary Science Letters 478 (2017) 47–57

Contents lists available at ScienceDirect

Earth and Planetary Science Letters

www.elsevier.com/locate/epsl

The source location of mantle plumes from 3D spherical models of mantle convection

Mingming Li *, Shijie Zhong

Department of Physics, University of Colorado, Boulder, CO, USA

ARTICLE INFO

Article history:
Received 20 October 2016
Received in revised form 17 April 2017
Accepted 24 August 2017
Available online 15 September 2017
Editor: B. Buffett

Keywords:
plume source location
large igneous province
lowermost mantle
LLSVP

ABSTRACT

Mantle plumes are thought to originate from thermal boundary layers such as Earth's core-mantle boundary (CMB), and may cause intraplate volcanism such as large igneous provinces (LIPs) on the Earth's surface. Previous studies showed that the original eruption sites of deep-sourced LIPs for the last 200 Myrs occur mostly above the margins of the seismically-observed large low shear velocity provinces (LLSVPs) in the lowermost mantle. However, the mechanism that leads to the distribution of the LIPs is not clear. The location of the LIPs is largely determined by the source location of mantle plumes, but the question is under what conditions mantle plumes form outside, at the edges, or above the middle of LLSVPs. Here, we perform 3D geodynamic calculations and theoretical analyses to study the plume source location in the lowermost mantle. We find that a factor of five decrease of thermal expansivity and a factor of two increase of thermal diffusivity from the surface to the CMB, which are consistent with mineral physics studies, significantly reduce the number of mantle plumes forming far outside of thermochemical piles (i.e., LLSVPs). An increase of mantle viscosity in the lowermost mantle also reduces number of plumes far outside of piles. In addition, we find that strong plumes preferentially form at/near the edges of piles and are generally hotter than that forming on top of piles, which may explain the observations that most LIPs occur above LLSVP margins. However, some plumes originated at pile edges can later appear above the middle of piles due to lateral movement of the plumes and piles and morphologic changes of the piles. ~65–70% strong plumes are found within 10 degrees from pile edges in our models. Although plate motion exerts significant controls over the large-scale mantle convection in the lower mantle, mantle plume formation at the CMB remains largely controlled by thermal boundary layer instability which makes it difficult to predict geographic locations of most mantle plumes. However, all our models show consistently strong plumes originating from the lowermost mantle beneath Iceland, supporting a deep mantle plume origin of the Iceland volcanism.

1. Introduction

Hotspots are commonly observed away from plate boundaries. Although different mechanisms have been proposed for the formation of hotspots, many hotspots show deep-sourced features and may be caused by mantle plumes (Courtillot et al., 2003; Morgan, 1971). An anomalously hot and large head of a mantle plume is often suggested to cause large igneous provinces (LIPs) with extremely large accumulations of igneous rocks on the Earth's surface (Campbell and Griffiths, 1992). The location of deep-sourced LIPs is largely determined by the source location of mantle plumes, which is itself controlled by the dynamics in the thermal boundary layer (TBL), such as that above the core-mantle boundary (CMB). The distribution of LIPs on the Earth's surface thus provides important constraints on the physical parameters, structure and dynamics of the lowermost mantle. In addition, mantle plumes bring materials from the deep mantle to the surface. The source location and composition of mantle plumes provide insights into the distribution of compositional reservoirs in the deep mantle (e.g., Hofmann, 1997; Li et al., 2014; Williams et al., 2015).

One prominent feature for the seismic structure of the lowermost mantle is the two large low shear velocity provinces (LLSVPs) beneath Africa and Pacific, which are surrounded by regions with higher than average seismic velocities (e.g., Dziewonski et al., 2010). The LLSVPs are suggested to be compositionally distinct from the surrounding mantle, based on seismic observations (e.g., Ishii and Tromp, 1999; Ni et al., 2002; Wen et al., 2001). Geodynamic modeling studies indicate that the LLSVPs may be caused by thermochemical piles of compositionally distinct and

* Corresponding author.
E-mail address: Mingming.Li@colorado.edu (M. Li).

http://dx.doi.org/10.1016/j.epsl.2017.08.033
0012-821X/

intrinsically dense material (e.g., McNamara and Zhong, 2005; Zhang et al., 2010), although a purely thermal origin of LLSVPs cannot be ruled out yet (Bull et al., 2009; Davies et al., 2012; Schubert et al., 2004, 2009). Interestingly, Torsvik et al. (2006) found that the original eruption sites of most LIPs younger than ~200 Myrs appear to be located preferentially above the edges of the LLSVPs. Although it was also suggested that several LIPs older than 200 Myrs were located above the edges of LLSVPs (Torsvik et al., 2010, 2008), their evidence is not as robust (Zhong and Liu, 2016). The statistical significance of the spatial correlation between LIPs and the margins of LLSVPs has also been debated (Austermann et al., 2014; Davies et al., 2015; Doubrovine et al., 2016).

The source locations of mantle plumes are not fully understood in previous geodynamic studies. Tan et al. (2011) computed 3D convection models with temperature- and depth-dependent viscosity and free-slip surface boundary condition for a long geological time (~1 billion years) and found that mantle plumes form both at pile edges, in the middle of the top surface of piles, and far outside of the piles. Hassan et al. (2015) examined the correlation of modeled plume eruption sites with the reconstructed LIP eruption sites using geodynamic models with plate motion history and similar mantle rheology to that in Tan et al. (2011). They found that the correlation between plume locations and LIP eruption sites is better for thermochemical models than for isochemical models. Similar to Tan et al. (2011), they found mantle plumes erupt both near the edges and on the top of thermochemical piles. Steinberger and Torsvik (2012) reproduced the observed trend of plume locations at the LLSVP's edges using simplified geodynamic models with plate subduction history, but they did not examine effects of important model parameters such as the viscosity and other thermodynamic parameters (i.e., thermal expansivity and thermal diffusivity). In addition, the physical parameters they used in the models lead to a small Rayleigh number and sluggish mantle convection. Since their models were computed for a relatively short time of 300 Myrs, they showed that their modeling results are sensitive to initial conditions. Furthermore, the models by Steinberger and Torsvik (2012) ignored the temperature-dependent viscosity, used relatively poor resolution (i.e., ~450 km horizontal resolution or for harmonic degrees up to 50) in the lower mantle, and only considered radial thermal diffusion in the equation of energy conservation. It is unclear how these simplifications would affect the plume dynamics in Steinberger and Torsvik (2012). Therefore, it remains critically important to investigate the controls on the source locations of mantle plumes, or more specifically, to examine the conditions under which the plumes form outside, near the edges of, or above the middle of LLSVPs. An improved knowledge on this question would not only help understand the spatial correlation between LIP eruption sites and LLSVP margins, but also provide additional tools to use the observations to constrain physical properties in the lowermost mantle.

In this study, we perform 3D spherical thermochemical and isochemical convection calculations with plate motion history to investigate the controls on the source locations of mantle plumes. We systematically examine the sensitivity of plume source locations to model parameters including viscosity, thermal expansivity, and thermal diffusivity in the mantle. Our models significantly expand the model parameter space compared to the previous studies on this topic (Tan et al., 2011; Hassan et al., 2015; Steinberger and Torsvik, 2012). We also compare numerical modeling results with theoretical scaling analyses (e.g., Olson, 1993; Zhong, 2005) to give a comprehensive understanding of the physical process that controls the source location of mantle plumes.

Table 1
Parameters used in this study.

Parameters	Reference value
Earth's radius R	6371 km
CMB radius	3503 km
Mantle density ρ_0	3300 kg/m^3
Thermal expansivity α_0	3×10^{-5} K^{-1}
Thermal diffusivity κ_0	1×10^{-6} m^2/s
Gravitational acceleration g	9.8 m/s^2
Temperature change across the mantle ΔT	2500 K
Reference viscosity η_0	3×10^{21} Pa s, 6×10^{21} Pa s or 1.5×10^{22} Pa s

2. Methods

We perform geodynamic calculations by solving the following dimensionless equations of conservation of mass, momentum and energy under the Boussinesq approximation:

$$\nabla \cdot \vec{u} = 0, \tag{1}$$

$$-\nabla P + \nabla \cdot (\eta \dot{\epsilon}) = Ra(\alpha T - BC)\hat{r}, \tag{2}$$

$$\frac{\partial T}{\partial t} + (\vec{u} \cdot \nabla)T = \nabla \cdot (\kappa \nabla T) + Q, \tag{3}$$

where $\vec{u}$ is the velocity, P is the dynamic pressure, η is the viscosity, $\dot{\epsilon}$ is the strain rate, Ra is the Rayleigh number, T is the temperature, B and C are the buoyancy number and composition, respectively. $\hat{r}$ is the unit vector in the radial direction, t is the time, Q is the internal heating rate. α and κ are thermal expansivity and thermal diffusivity, respectively. The convection models are similar to that in (McNamara and Zhong, 2005; Zhang et al., 2010; Li et al., 2016; Hassan et al., 2015).

The Rayleigh number (Ra) in equation (2) is defined as:

$$Ra = \frac{\rho_0 g \alpha_0 \Delta T R^3}{\eta_0 \kappa_0}, \tag{4}$$

where ρ_0, g, α_0, η_0 and κ_0 are the background mantle reference density, the gravitational acceleration, the reference thermal expansivity, the reference viscosity, and the reference thermal diffusivity, respectively. ΔT is the temperature difference between surface and CMB and R is the radius of the Earth. The reference values are listed in Table 1. In this study, we use a Rayleigh number of 2×10^8 for most cases (i.e., with a reference viscosity of 3×10^{21} Pa s). Because the Rayleigh number is defined using the radius of the Earth, it is about 10 times larger than that defined using the thickness of Earth's mantle.

The buoyancy number B in equation (2) is defined as the ratio of the intrinsic density anomaly of compositionally distinct materials $\Delta\rho$ to the density anomaly caused by thermal expansion:

$$B = \frac{\Delta \rho}{\rho_0 \alpha_0 \Delta T}. \tag{5}$$

The advection of the composition C is given by:

$$\frac{\partial C}{\partial t} + (\vec{u} \cdot \nabla)C = 0. \tag{6}$$

The mantle viscosity is both temperature- and depth-dependent and is similar to that in (Zhang et al., 2010). The viscosity is expressed as $\eta = \eta_0 \exp[A(0.5 - T)]$, where the activation energy $A = 9.21$ is chosen such that there is 10^4 viscosity variation due to changes of non-dimensional temperature from 0 to 1. The viscosity pre-factor η_0 is depth-dependent, with $\eta_0 = 1.0$ for the uppermost 150 km, and $\eta_0 = 1/30$ between 150 and 670 km. Our models also include a ~60 times viscosity increases across the 670-km depth from the upper mantle to lower mantle, and a factor of ~3.4 viscosity linear increase from the 670-km depth to CMB. All cases

Table 2
Cases used in this study.

Case	α	κ	B	Ra	d (km)	η_l (Pa s)	Ra_l
1	1.0	1.0	0.48	2e8	47	3.3e21	41
2	0.2	2.18	0.18	2e8	79	2.4e21	23
3	1.0	1.0	0.52	4e7	66	1.7e22	23
4	0.2	1.0	0.18	2e8	63	2.7e21	24
5	1.0	2.18	0.48	2e8	59	2.6e21	45
6	1.0	1.0	0.50	1e8	56	6.5e21	38
7	0.33	2.18	0.23	2e8	73	2.4e21	31
8	0.33	2.18	0.24	1e8	84	5.1e21	23
9	0.33	2.18	0.26	4e7	–	–	–
10	0.2	2.18	–	2e8	–	–	–

α and κ are the non-dimensional thermal expansivity and thermal diffusivity at CMB, respectively; B is buoyancy number; Ra is global Rayleigh number; d is the thickness of TBL outside thermochemical piles; η_l is the viscosity at middle depth of the TBL outside of thermochemical piles; Ra_l is the local Rayleigh number of the TBL outside of thermochemical piles.

used in this study are listed in Table 2. The present-day depth profiles of the horizontally averaged viscosity for Cases 1, 3 and 6 with different Rayleigh number (e.g., difference reference viscosity) are shown in Supplementary Fig. S1.

Temperature boundary condition is isothermal on the surface ($T = 0$) and the CMB ($T = 1$). We use a dimensionless internal heating rate of $Q = 100$, which results in about 50–70% internal heating ratio, consistent with previous studies based on constraints from plume heat flux and plume excess temperature (Leng and Zhong, 2008; Zhong, 2006), although the effects of internal heating are generally small on a relative short time scale as in this study.

The CMB has a free-slip velocity boundary condition, but the surface employs a kinematic velocity boundary condition with time-dependent plate motion. All models are run from 458 Ma to the present day. The plate motion history from 458 Ma to 225 Ma is derived from Zhang et al. (2010). From 200 Ma to present day, we use the plate motion model from Seton et al. (2012). For the period of 225–200 Ma, we use the plate motion model from Seton et al. (2012) at 200 Ma. Because the plate motion model is less robust the further back in time, we focus on analyzing model results for the past 180 Myrs.

For thermochemical calculations, the initial temperature is the same as that used in Zhang et al. (2010), which is a 1-D average temperature profile from a pre-calculation with intrinsically dense material in the lowermost mantle until quasi-equilibrium is achieved. Initially, we introduce a global layer of intrinsically dense material in the lowermost 250 km of the mantle. For isochemical calculations, the increase of temperature in the lowermost mantle is removed from the initial 1D temperature profile.

We solve the governing equations (i.e., equations (1)–(3) and (6)) using the finite element code CitcomS (Zhong et al., 2008). The dimensionless radius of the computational domain ranges from 0.55 at the CMB to 1.0 at the surface. The entire mantle is modeled as a 3D spherical shell, which is divided into 12 caps with each cap containing $64 \times 64 \times 64$ elements. The lateral resolution in the lowermost 300 km depth is about 55–60 km, and the grids are refined in this depth range to a radial resolution of ~24 km. The radial grids are not refined from surface to 300 km depth above the CMB.

The primary goal of this study is to understand the controls on the plume source locations. Although mantle plumes may tilt and merge as they ascend through the mantle, we will mainly focus on quantifying mantle plumes near their source locations at the CMB. A number of previous studies attempted to quantify mantle plumes for their population and energy flux (e.g., Labrosse, 2002; Zhong, 2005; Leng and Zhong, 2008), and our method for quantifying the number of plumes is similar to these studies. We define plumes as the regions where the temperature anomaly is higher than a threshold value (e.g., 0.1). When the distance between two plumes is less than 3 degrees, we consider them as one plume. When computing number of plumes outside of thermochemical piles, we exclude those with distance smaller than 3 degrees from the edges of piles. The number of plumes depends moderately on the criteria in defining plumes (e.g., Labrosse, 2002), so we focus on the relative difference of plume numbers between models.

3. Results

3.1. Mantle plumes outside of thermochemical piles

We first show how mantle viscosity, thermal expansivity and thermal diffusivity control the plume population outside of the thermochemical piles. Case 1, as the reference case, uses constant thermal expansivity α and thermal diffusivity κ. It employs a buoyancy number of $B = 0.48$ for the intrinsically dense material, leading to thermochemical piles covering similar area extent of the CMB as the LLSVPs do. Fig. 1a shows the present-day temperature anomaly (i.e., after the horizontal average temperature is removed) at 2800-km depth. The black contours show two thermochemical piles: one pile in the middle of the map is beneath Africa (hereinafter referred to as Africa pile) and the other pile is beneath the Pacific (hereinafter referred to as Pacific pile). The thermochemical piles are generally much hotter than the surrounding mantle. We find that mantle plumes frequently form in relatively cold regions outside of the piles for this case (Fig. 1a).

The cyan arrows in Fig. 1a show the lateral mantle flow velocity at 2800 km depth. Materials outside the piles are generally being advected towards the edges of piles (Fig. 1a). It is interesting to note that mantle flow locally converges at the north end of the Africa pile (Fig. 1a). Fig. 1b shows the corresponding magnitude of lateral flow velocity, with green contours for temperature anomaly of 0.1 showing locations of mantle plumes. These mantle plumes are preferentially located in regions where mantle lateral flow velocity either changes rapidly (i.e., large velocity gradient) or has a small amplitude (i.e., stagnation points in Zhong et al. (2000)). The number of plumes outside of piles, quantified using criteria discussed above, changes with time and ranges from 10 to 20 in the past 180 Myrs for Case 1 (Fig. 2a, black line).

In Case 2, the thermal expansivity is decreased and the thermal diffusivity is increased from the surface to CMB by a factor of 5 and 2.18, respectively. The depth-dependent thermodynamic properties are more consistent with mineral physics results (Hofmeister, 1999) and have been adopted in previous numerical studies (e.g., Leng and Zhong, 2008; Tackley, 2002). The buoyancy number for this case is reduced to 0.18 to produce a similar area extent of thermochemical piles as in Case 1. Case 2 is otherwise identical to Case 1. We find that mantle plumes outside of the piles in Case 2 (Fig. 3a) are larger in size than that in Case 1 (Fig. 1a). However, compared to Case 1, the number of plumes occurring outside of piles is much less in Case 2. During the past 180 Myrs, the number of plumes outside of the piles is generally less than 3 (Fig. 2a, red line).

In Case 3 (Table 2), the reference viscosity is 5 times of that for Case 1 with a Rayleigh number of $Ra = 4 \times 10^7$, and the buoyancy number is increased to 0.52 to keep similar size of the piles to the previous cases. As expected for higher mantle viscosity, the mantle convection is more sluggish and mantle flow velocity in most regions (Fig. 3b) is smaller than that in Cases 1 (Fig. 1a) and 2 (Fig. 3a). However, the mantle convection pattern remains the same, with materials outside of the piles generally being advected towards pile edges. The plumes outside of piles for Case 3 have a relatively large size (Fig. 3b), but the number of plumes is generally no more than 5 for the past 180 Myrs (Fig. 2a, blue line).

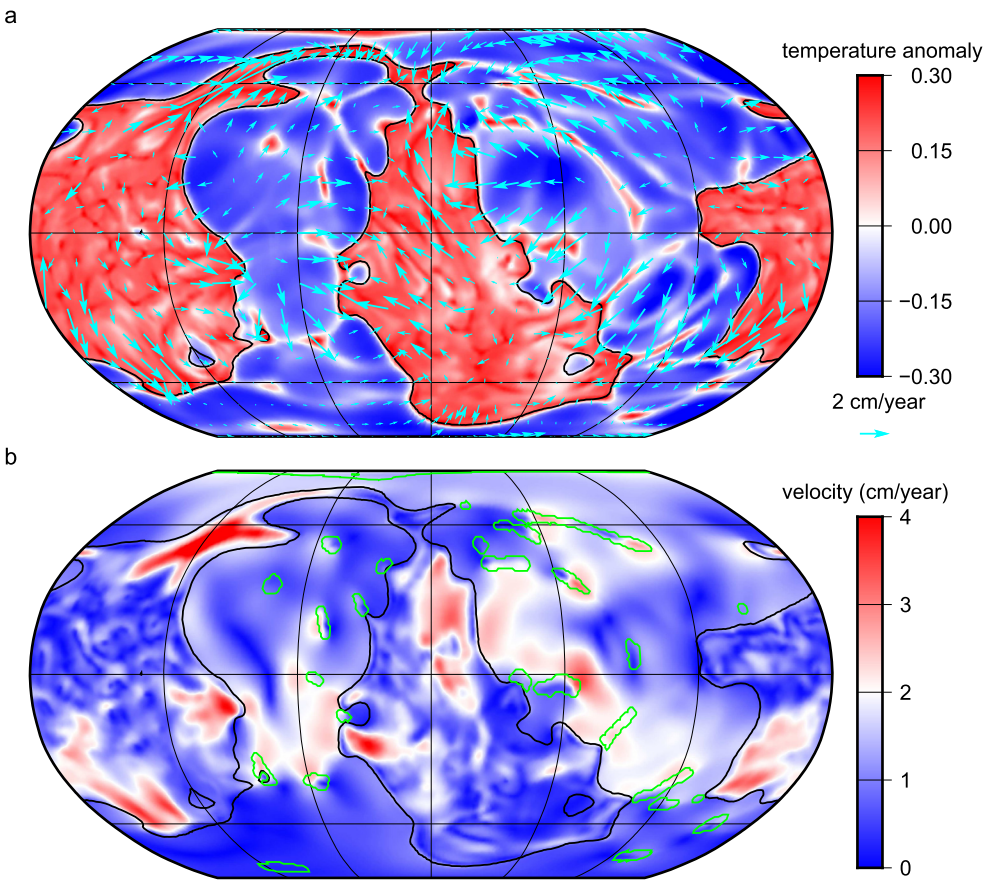

Fig. 1. (a) Present-day temperature anomaly at 2800 km depth for Case 1 after the horizontal average is removed. The cyan arrows show lateral mantle flow velocity at this depth. (b) Magnitude of lateral velocity as shown in panel (a). The green contours of temperature anomaly of 0.1 show location of mantle plumes at 2800 km depth. The black lines in panels (a) and (b) show edges of thermochemical piles. The figures are centered at longitude = 0°. (For interpretation of the references to color in this figure legend, the reader is referred to the web version of this article.)

Case 4 differs from Case 1 in only having a linear decrease in thermal expansivity from 1.0 at the surface to 0.2 at the CMB (i.e., thermal diffusivity remains uniform in the mantle, Table 2). For this case, no more than 4 plumes are found outside of the piles for the past 180 Myrs (Fig. 2a, green line). In Case 5, the thermal expansivity is constant, but thermal diffusivity is increased from the surface to the CMB by a factor of 2.18 (Table 2). The number of plumes outside of the piles for this case (Fig. 2a, cyan line) is slightly less than that in Case 1 for most of the time. Case 6 uses a reference mantle viscosity that is twice of that for Case 1, leading to a Rayleigh number of $Ra = 10^8$ for Case 6 (Table 2). For this case, the number of plumes outside of piles is slightly less than that in Case 1 before ∼30 Ma, and is ∼7 after ∼30 Ma (Fig. 2a, orange line).

We also explored cases (Cases 7–9, Table 2) with a smaller reduction of thermal expansivity (i.e., a factor of three) with depth than Case 2. The differences among Cases 7–9 are that the Rayleigh number Ra is systematically reduced from $Ra = 2 \times 10^8$ for Case 7, to 10^8 for Case 8, and to 4×10^7 for Case 9. The number of plumes outside of piles for Case 7 is higher than that in Case 2, but is much lower than that in Case 1, and it further decreases in Case 8 where the reference viscosity is increased to twice that of Case 7 (Fig. 2a). However, we find that the mantle convection for Case 9 is much more sluggish than other cases, and the results of Case 9 are significantly affected by initial condition (see Supplementary Information and Supplementary Fig. S3 for more details). We thus do not quantify the results of Case 9.

3.2. Mantle plumes above and at the edges of thermochemical piles

We next investigate the location of mantle plumes above the middle of the top surface of the thermochemical piles and at the edges of the piles. As an example, we show and compare the results for Case 1 and Case 2 in which the overall morphologies of thermochemical piles are similar. Figs. 4a and 4b show the present-day temperature anomaly at ∼1500 km depth for Cases 1 and 2, respectively, and the green contours of temperature anomaly of 0.1 represent mantle plumes. The number of plumes outside of piles at this depth is less than that near the CMB as shown in Figs. 1a and 3a because several plumes have not reached this depth yet. In addition, weak plumes may diffuse out on their way up to the surface because of limited resolution of our models. Strong plumes with maximum temperature anomaly larger than 0.2 are marked by black dots to distinguish them from other relatively weaker plumes.

Fig. 4a shows that there are many more plumes occurring at the edges and above the middle of thermochemical piles than outside of piles for Case 1. We find a frequent occurrence of weak plumes above the middle of thermochemical piles, with small spacing between these plumes. However, most of the strong plumes are closer to the pile edges, similar to Tan et al. (2011).

For Case 2 with depth-dependent thermal expansivity and diffusivity, we find that there are much less plumes not only outside of the piles but also associated with thermochemical piles than Case 1 (Figs. 2a, 3a, and 4b). In addition, the spacing between plumes on top of the piles is larger than that in Case 1. Similar to Case 1, we find that strong plumes preferentially locate near

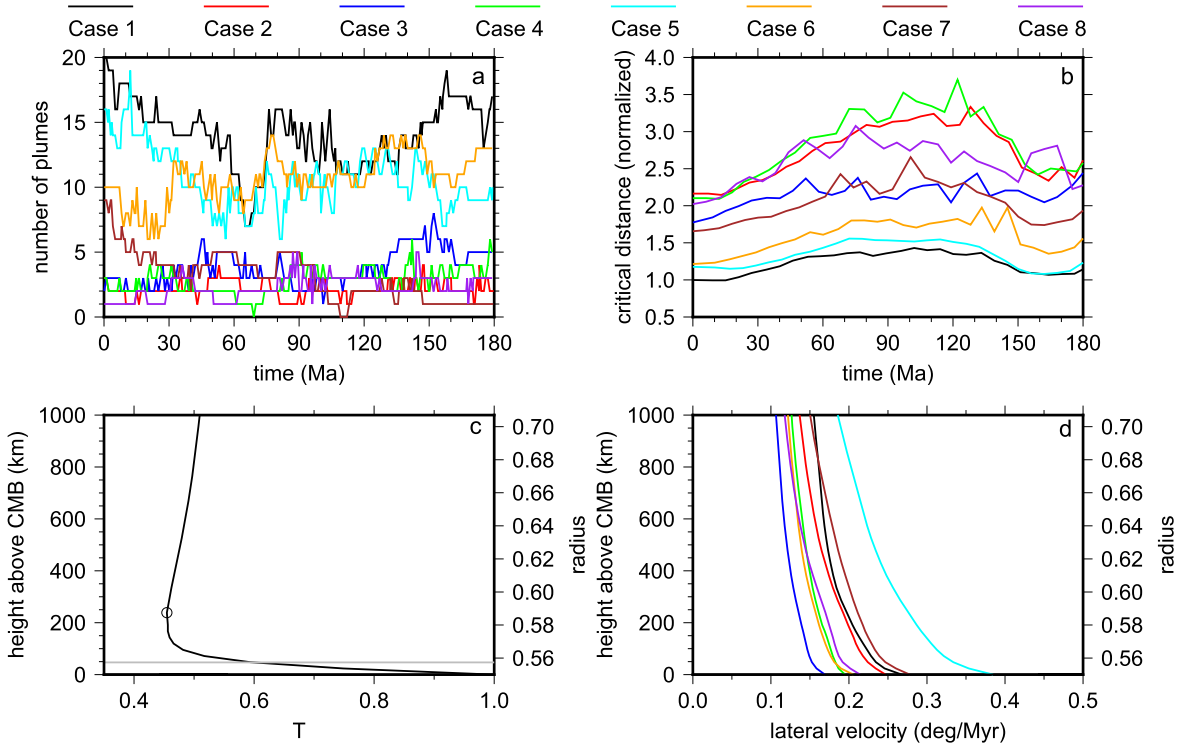

Fig. 2. Time evolution of number of plumes occurring outside of thermochemical piles (a) and the critical distance that is required for the TBL to grow thick enough to produce plumes (b) for Cases 1 to 8. The critical distance for each case is normalized by the critical distance for Case 1 at present-day. (c) Laterally averaged temperature outside thermochemical piles (including regions at pile edges) in the past 40 Ma (solid black line) for the Case 1. The gray line shows the radius of the top of the TBL quantified using equation (12). The black open circle marks the depth with minimum average temperature. (d) Horizontally averaged magnitude of the lateral mantle flow velocity outside of piles in the past 40 Ma for Cases 1 to 8. (For interpretation of the references to color in this figure, the reader is referred to the web version of this article.)

the pile edges (e.g., <10 degrees from the pile edges), while weak plumes tend to cluster above the middle of the piles (e.g., >10 degrees from the pile edges).

We quantify the minimum distances to pile edges for the strong plumes at 2800 km depth in the past 180 Myrs in Cases 1 and 2. We find that most (~65–70%) strong plumes are located within ~10 degrees from the pile edges for both cases. A significant number of strong plumes occur just above the pile edges (i.e., ~0 degree) for Case 1 (Fig. 4c), and at 5–10 degrees for Case 2 (Fig. 4d).

Fig. 5 shows four snapshots of the temperature anomaly field at 1500 km depth for Case 2 from 85 Ma to 0 Ma (i.e., the present-day). Most strong plumes occur near the edges of piles for all snapshots. At 85 Ma, plumes A and B are located near the edges of the Africa pile. From 85 Ma to 0 Ma, the Africa pile changes its shape and moves northwestern, and the two plumes slightly move westward. As a result, the two plumes appear above the middle of the Africa pile at the present-day. In addition, the temperature of plume B decreases with time such that it no longer meets the criteria for strong plumes at the present-day. A strong mantle plume forming on top of the end tail of the Africa pile moves westward with the pile from ~85 Ma to present-day, and it is less than 10 degrees from beneath Iceland at the present-day. In fact, strong plumes are found close to the location beneath Iceland in other models as well (Fig. 4a, b; Supplementary Fig. S2).

3.3. Plume source location for isochemical model

The origin of LLSVPs remains enigmatic and a purely thermal origin of LLSVPs, as in the conventional isochemical mantle model (e.g., Hager et al., 1985), may remain viable (Bull et al., 2009; Davies et al., 2012; Schubert et al., 2004, 2009). Here, we perform another calculation (Case 10) to explore the plume source location in an isochemical model. All parameters used in Case 10 are the same as Case 2, but there is no intrinsically dense material in Case 10.

In contrast to the large-scale temperature anomalies for thermochemical models (i.e., Figs. 1a and 3), the temperature field at 2800 km depth for Case 10 is featured by relatively small scale interconnected hot anomalies separated by cold regions (Fig. 6a), similar to that found in previous studies (e.g., Zhong et al., 2000; Bull et al., 2009). All plumes shown at 1500 km depth (Fig. 6b) are strong plumes, which seem to be evenly distributed in regions away from cold downwellings. Similar to the thermochemical models, we find that mantle flow locally converges in the lowermost mantle (Fig. 6a) beneath Iceland (black triangle). A strong plume is found not too far from beneath Iceland.

4. Discussion

4.1. Understanding geodynamic modeling results on plume source location

The geodynamic modeling results on plume source location can be understood in a more theoretical way, based on thermal boundary layer (TBL) instability theory (e.g., Olson, 1993; Zhong, 2005). The formation of mantle plumes from TBL is controlled by the local Rayleigh number, which is defined by:

$$Ra_l = \frac{\rho_0 g \alpha_l \Delta T_l \delta^3}{\eta_l \kappa_l}, \tag{7}$$

where α_l, ΔT_l, δ, η_l, and κ_l are thermal expansivity, temperature different across the TBL, thickness of the TBL, viscosity and thermal diffusivity, respectively. All parameters are defined locally for the TBL. The TBL becomes unstable to form plumes when the lo-

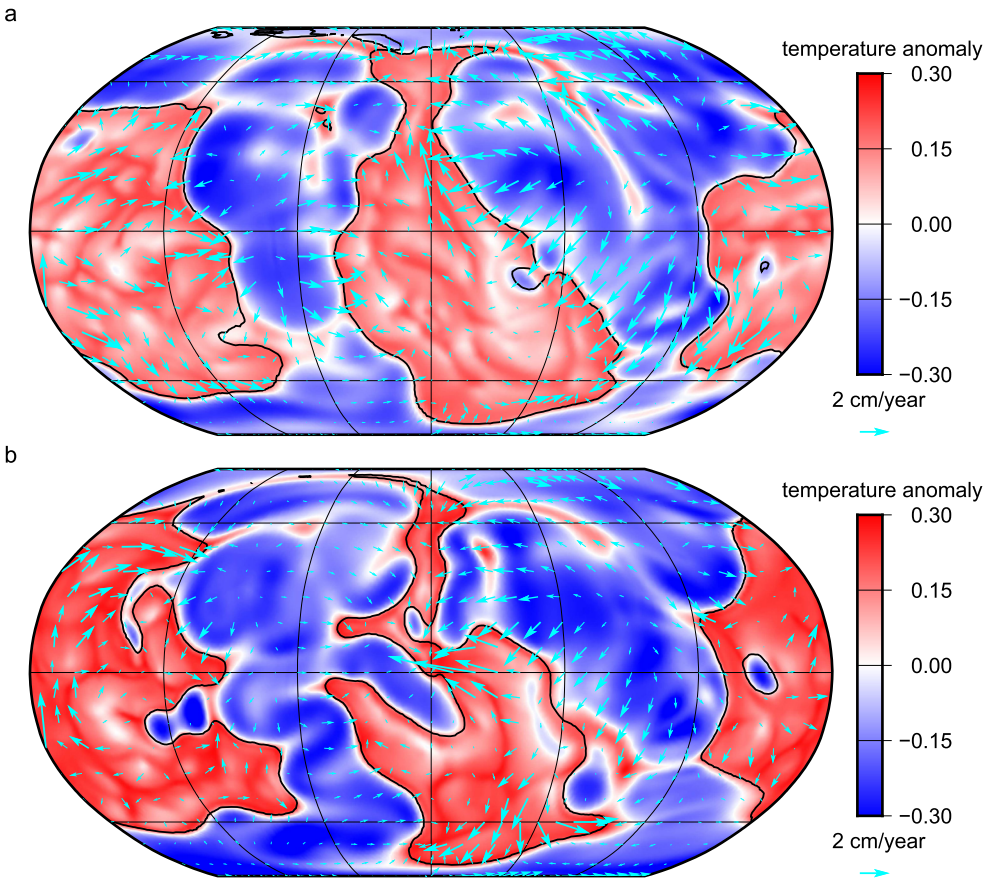

Fig. 3. Present-day temperature anomaly at 2800 km depth for Case 2 (a) and Case 3 (b). The cyan arrows show lateral mantle flow velocity. The black lines show edges of thermochemical piles. The figures are centered at longitude = 0°. (For interpretation of the references to color in this figure legend, the reader is referred to the web version of this article.)

cal Rayleigh number reaches a critical Rayleigh number Ra_c (e.g., Howard, 1966):

$$Ra_l = Ra_c = \frac{\rho_0 g \alpha_l \Delta T_l d^3}{\eta_l \kappa_l}, \tag{8}$$

where d is the TBL thickness required to form plumes.

The process of forming mantle plumes on the CMB is illustrated in Fig. 7. The thickness of TBL δ is minimum beneath the slab and increases with time due to thermal diffusion as the slab material spreads in the mantle flow direction above the CMB. We may define the distance between the downwelling with minimum δ and where the plume forms as L. If L is shorter than the distance to pile edges, mantle plumes would form outside of and far away from the thermochemical piles. Otherwise, the TBL could only be thick enough at the edges of piles (where mantle flow changes its direction) to form plumes. We hereinafter define the distance L as the critical distance. The critical distance is controlled by 1) the time it takes to form mantle plumes t_{pf} and 2) the magnitude of lateral mantle flow velocity in the TBL U, thus:

$$L = U t_{pf}. \tag{9}$$

The plume formation time can be related to the critical Rayleigh number Ra_c through the following way. The TBL thickens with time through:

$$\delta = \sqrt{c \kappa_l t}, \tag{10}$$

where c is a constant. At $t = t_{pf}$, the TBL thickness is $\delta = d$, or $d = \sqrt{c \kappa_l t_{pf}}$. Plugging this equation into equation (8) and rearranging it, we get:

$$t_{pf} = \frac{1}{c \kappa_l^{1/3}} \left(\frac{Ra_c \eta_l}{\rho_0 g \alpha_l \Delta T_l} \right)^{2/3}. \tag{11}$$

One question is what is the value of Ra_c and whether it is a constant in our different geodynamic models for the development of TBL instability. To answer this question, we further quantify the critical Rayleigh number outside of thermochemical piles in Cases 1 to 8. We first determine the thickness of TBL, using the CMB heat flux and interior temperature (Moresi and Solomatov, 1995). As an example, Fig. 2c shows the laterally averaged temperature profile (solid black line) outside of the piles for the last 40 Ma for Case 1. The dimensionless thickness of TBL is computed by (Moresi and Solomatov, 1995):

$$d = \frac{k_l (1 - T_i)}{q_{cmb}}, \tag{12}$$

where k_l is the non-dimensional thermal conductivity whose value is the same as the non-dimensional thermal diffusivity κ_l, q_{cmb} is the average non-dimensional CMB heat flux outside of thermochemical piles, and T_i is the interior temperature that is set to be the minimum temperature on the laterally averaged temperature profile in the lowermost mantle (e.g., marked by black circle in Fig. 2c). We also used a temperature gradient based method in Liu and Zhong (2013) to determine the thickness of the TBL and the results are similar to those from (12).

We compute the laterally averaged temperature and viscosity outside of piles (including regions at pile edges) for the past 40 Ma for Cases 1 to 8, and the average temperature profile is used to calculate the TBL thickness for each case with equation (12). Table 2 lists the TBL thickness and the average viscosity at middle depth of

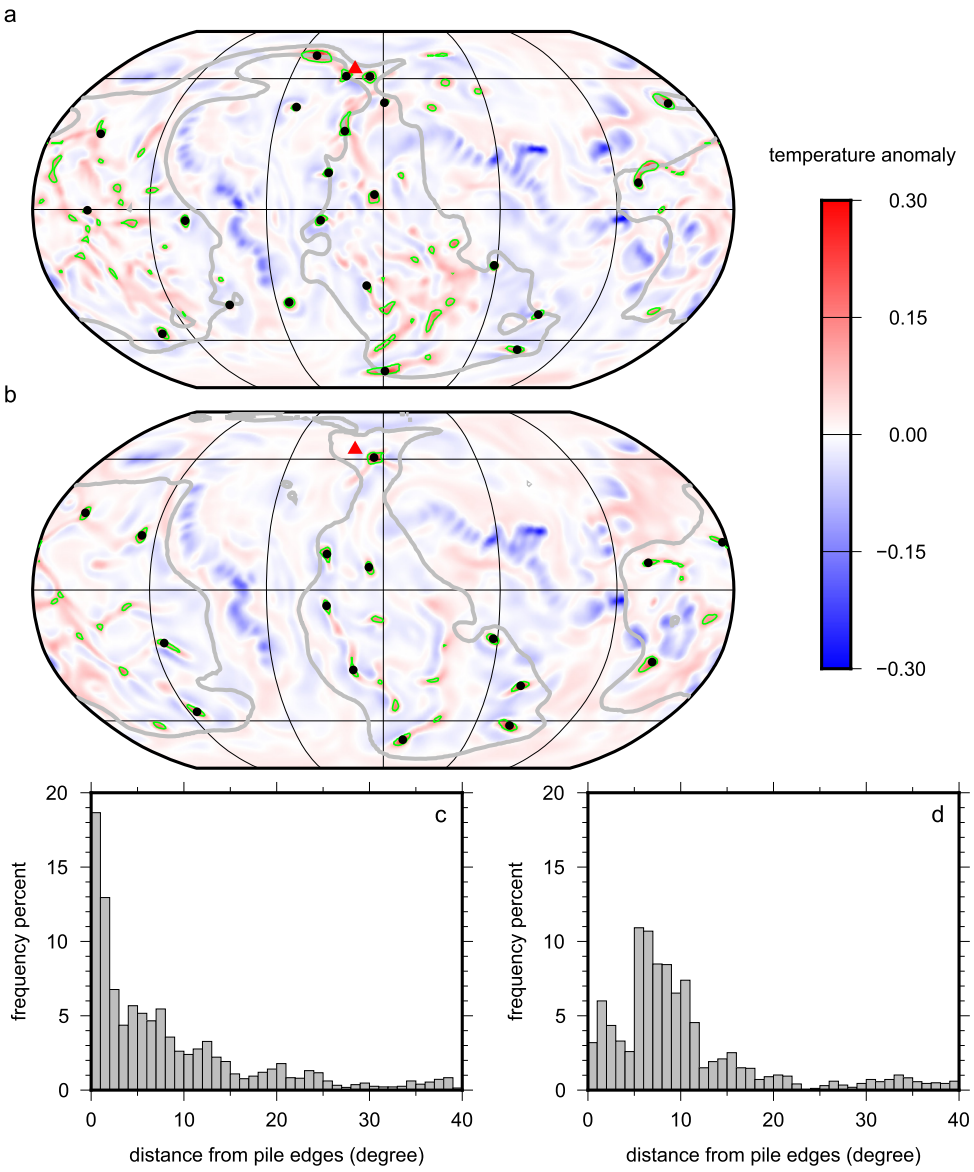

Fig. 4. Present-day temperature anomaly at 1500 km depth for Case 1 (a) and Case 2 (b). The gray lines show the edges of thermochemical piles at 2800 km depth. The green contours of temperature anomaly at 0.1 show locations of mantle plumes. The black dots show locations of strong plumes whose maximum temperature anomaly is larger than 0.2. The red triangles in panels (a) and (b) show the location of the Iceland. The figures are centered at longitude = 0°. (c)–(d), histograms of number of strong plumes as a function of distance from the closest edges of thermochemical piles for Case 1 (c) and Case 2 (d). We quantify the distances for strong plumes every 1 Myr in the past 180 Myrs, including 2768 and 2667 plumes in total for Case 1 and Case 2, respectively. (For interpretation of the references to color in this figure legend, the reader is referred to the web version of this article.)

the TBL, which are used to compute Ra_l for each case with equation (8). Despite of the complexities with the lowermost mantle dynamics in our 3D models and the large differences in physical parameters among these models, Ra_l is found in the range of ~20–40 for all these cases (Table 2). This range of Ra_l is similar to the critical Rayleigh number of ~30 derived from a marginal stability analysis for the TBL by Jaupart et al. (2007), supporting the hypothesis that the TBL dynamics and plume formation are controlled by the TBL instability.

However, because the value of constant c in equation (11) is unknown, it is difficult to estimate plume formation time t_{pf} directly from equations (11). We thus focus on quantifying the ratio of t_{pf} between models. From equation (11), we find that by decreasing the thermal expansivity by 5 times while increasing the thermal diffusivity by 2.18 times in the lowermost mantle in Case 2, the plume formation time for Case 2 would be increased by ~2.3 times compared to Case 1, assuming other parameters in equation (11) (e.g., η_l, ΔT_l) are the same for both cases. Similarly, we find that the plume formation time for Cases 3, 4, 5, 6, 7 and 8 is about 2.9, 2.9, 0.8, 1.6, 1.6, and 2.6 times that of Case 1, respectively.

Similarly, we also quantify the ratios of critical distance L for different cases relative to Case 1. We first determine the magnitude of lateral mantle flow velocity outside of piles on the CMB at different times in the last 180 Ma for Cases 1 to 8, which is then multiplied by the ratio of plume formation time between each case and Case 1 to obtain the time evolution of the critical distance ratios (e.g., Equation (9)). The critical distance ratio for different case at different times is further normalized by that of Case 1 at the present-day. Interestingly, the magnitude of lateral mantle flow velocity does not change significantly in the TBL for each case and, more importantly, the ratio of lateral mantle flow velocity between any two cases is nearly the same at different depths in the lowermost mantle (i.e., Fig. 2d). The normalized critical distance is thus

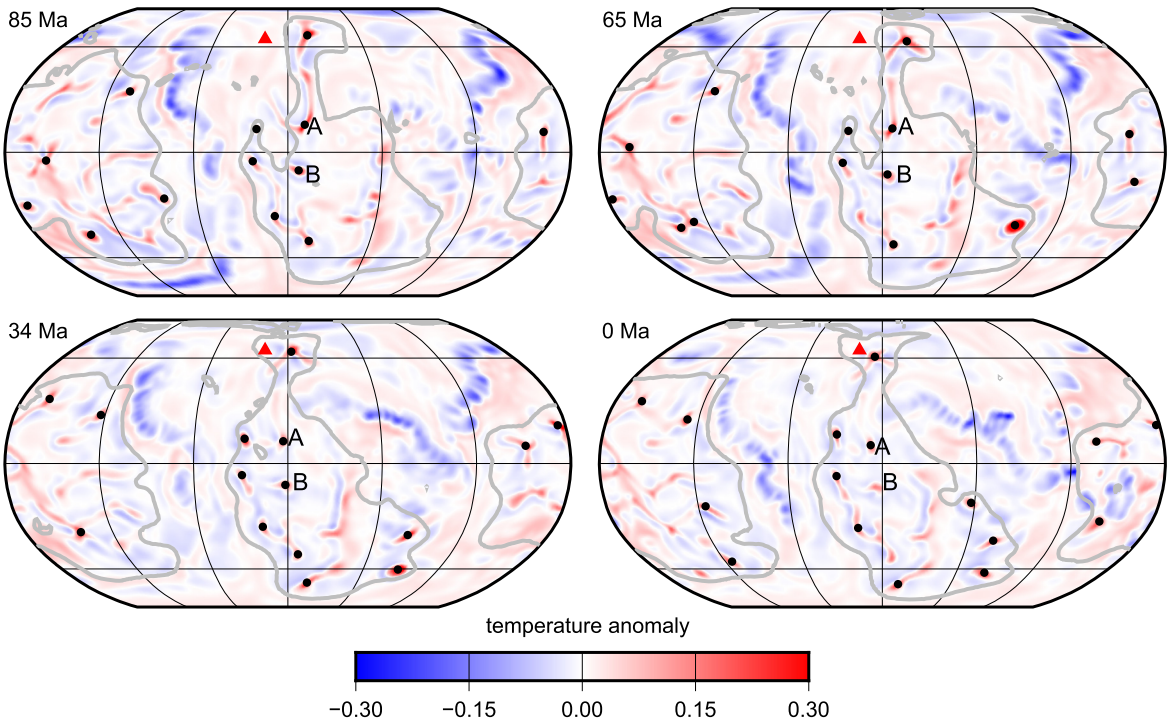

Fig. 5. Snapshots of temperature anomaly at 1500 km depth for Case 2. The gray contours show the edges of thermochemical piles at 2800 km depth. The black dots show locations of strong plumes whose maximum temperature anomaly is higher than 0.2. The symbols A and B show locations of plumes which are discussed in the text. The red triangles show the location of the Iceland. The figures are centered at longitude = 0°. (For interpretation of the references to color in this figure legend, the reader is referred to the web version of this article.)

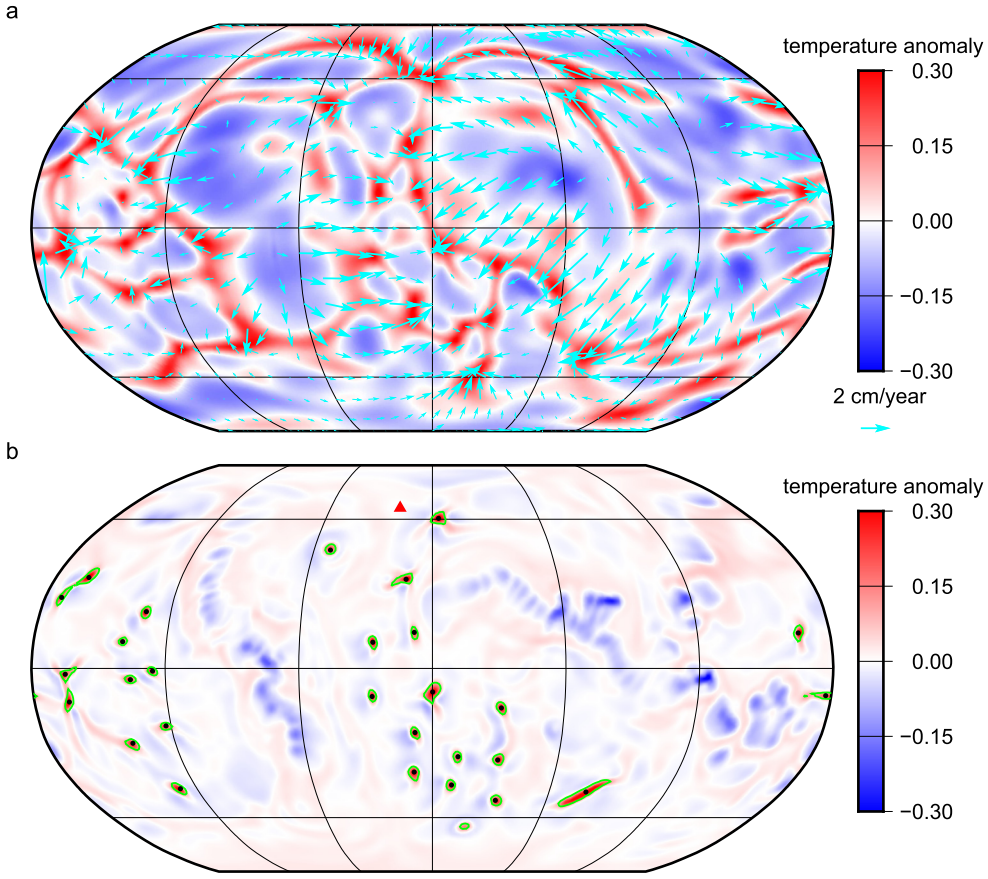

Fig. 6. (a) Temperature anomaly at 2800 km depth for Case 10 at the present-day, with lateral mantle flow velocity superimposed (cyan arrows). (b) temperature anomaly at 1500 km at the present-day for Case 10. The green contours of temperature anomaly at 0.1 show locations of mantle plumes. The black dots show the location of strong plumes whose maximum temperature anomaly is larger than 0.2. The red triangles in panels (b) show the location of Iceland. The figures are centered at longitude = 0°. (For interpretation of the references to color in this figure legend, the reader is referred to the web version of this article.)

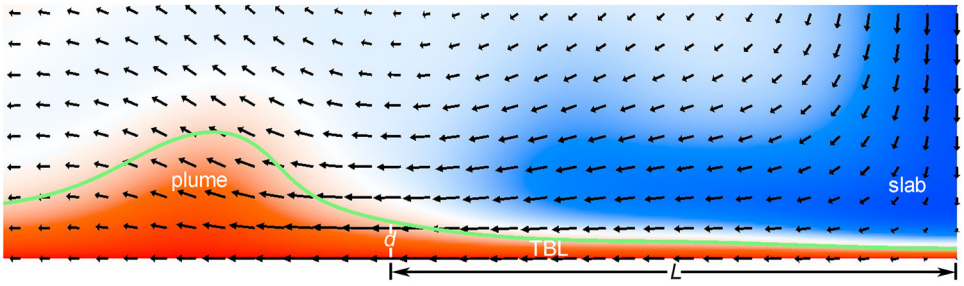

Fig. 7. The process of forming a mantle plume from a thermal boundary layer. Red and blue regions are hot and cold, respectively. Arrows show mantle flow velocity. The mantle plume forms after the thickness of TBL increases to d. L is the distance between the location where the thickness of TBL reaches d and the location where the TBL is thinnest (i.e., below the cold slab). The green line is an isotherm which outlines the top of the TBL. The temperature and velocity field in this figure are derived from a 2D mantle convection calculation. (For interpretation of the references to color in this figure legend, the reader is referred to the web version of this article.)

not affected by at what depth the magnitude of lateral mantle flow velocity is used.

Fig. 2b summarizes the time evolution of normalized critical distance for Cases 1 to 8, together with Fig. 2a showing the time evolution of number of plumes outside of piles. The critical distances for Cases 1, 5 and 6 are the shortest among the 8 cases, which is consistent with the largest number of plumes occurring outside of piles for these three cases. The critical distances for Cases 2, 4 and 8 are the longest and these cases have the smallest number of plumes outside piles. Cases 3 and 7 have intermedium critical distance and this is also consistent with the number of plumes in these cases. However, since the critical distance is based on the average temperature and mantle flow velocity in broad regions outside of thermochemical piles, we do not expect that all the details of plume population evolution can be predicted by the evolution of critical distance. Other factors, such as the changing morphology of thermochemical piles and changing of local mantle flow velocity due to subduction, may also influence the formation of plumes and hence the number of plumes. Nonetheless, we think that the critical distance helps understand the number of plumes forming outside of the piles, although the plume formation is in general controlled by the TBL instability.

The theory that we have developed to understand plume source locations outside of the piles also helps understand the formation of mantle plumes within and near the edges of piles. We find that for cases with less plumes outside of the piles, there are also less plumes above piles and these plumes have large spacing between them (Fig. 4a, b). This indicates that for cases in which the critical distance is large outside of the piles, it is also large on the top of the piles.

However, the dynamics on the top of the piles are different from outside of the piles above the CMB. Firstly, the TBL is thinnest beneath the cold downwellings outside of thermochemical piles; but there are no such strong downwellings on the top of the thermochemical piles. As a result, the TBL on top of piles thickens from a relatively large thickness, and it may need less time to become unstable to produce plumes. Secondly and perhaps more importantly, the top of the piles is not a free-slip boundary. Lateral mantle flow velocity on top of piles may be slower than that outside of piles on the free-slip CMB. Mantle flows may be stagnant in some localized regions on top of the piles due to the piles' topography. Thus, the critical distance may be much shorter on the top of the piles than outside of the piles, which is consistent with much more mantle plumes forming on top of the piles than outside of the piles.

4.2. Understanding the distribution of LIPs

Our results show that plumes forming at the edges of thermochemical piles are generally hotter than that forming on top of the piles (e.g., Tan et al., 2011). This can be understood through the following way. Mantle materials outside of the piles are advected towards the edges of thermochemical piles (Figs. 1a and 3), and the TBL outside of piles thickens in same direction as lateral mantle flow (Fig. 7) towards pile edges. If the TBL fails to become thick enough to produce plumes outside of piles, it may generate plumes at the edges of the piles which are physical barriers for the lateral movement of mantle flows. Thus, plumes forming at/near the edges of piles may partially contain materials from outside of the piles on the CMB. Because materials on the CMB are generally hotter than that on top of the piles (Farnetani, 1997), these plumes would be generally hotter than that forming on top of the piles.

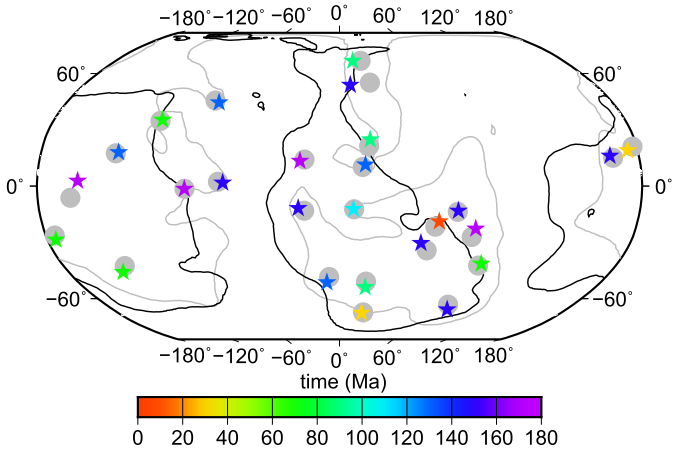

Fig. 8. The locations of initial arrivals of strong plumes at 300 km depth (stars) in the last 180 Ma. Strong plumes are plumes whose maximum temperature anomaly is higher than 0.2. The color of the stars represents the time when the plume initially reaches 300 km depth. For each plume location at 300 km depth (stars), the nearest gray circle shows the location of the plume conduit at 1500 km depth. The edges of thermochemical piles at 2800 km depth are shown at present-day (black contours) and at ~140 Ma (gray contours). (For interpretation of the references to color in this figure legend, the reader is referred to the web version of this article.)

It has been suggested that the eruption sites of LIPs preferentially occur above the margins of the LLSVPs (Torsvik et al., 2006, 2010), although the statistical significance of this spatial correlation has been debated (Austermann et al., 2014; Davies et al., 2015; Doubrovine et al., 2016). Although we find that strong mantle plumes preferentially form at/near the edges of thermochemical piles, as plumes ascend through the mantle, they are inevitably deflected by background mantle flow (Whitehead, 1982). To better understand the spatial correlation between the eruption sites of LIPs and the margins of LLSVPs, we show in Fig. 8 the locations of the initial arrivals of strong plumes at 300 km depth for Case 2 for the past 180 Ma, which may represent the eruption sites of LIPs. We find that plume conduits for ~80% of the plumes are deflected laterally by less than 500 km as plumes ascend from 1500 km depth to 300 km depth. Thus, the deflection of

plume conduits may not significantly affect the spatial correlation between LIP eruption sites and LLSVP edges.

However, the spatial correlation between plumes and present-day pile edges is affected by the changing morphology and location of piles in our geodynamic models. We find that although a plume tends to occur above the edges of thermochemical piles at the time when it initially reaches near the surface, it may be located well within or outside of the present-day thermochemical piles as the piles later change shape and location (Fig. 8). For example, two plumes that are formed at the longitude of about −120° during ∼120–160 Ma are above the edges of the Pacific pile (Fig. 8, the gray contours show the pile edges at 140 Ma). However, due to the changes of shape and location of the Pacific pile, at the present-day, these two plumes are outside of the piles (Fig. 8, black contour). Therefore, the significance of spatial correlation between LIP eruption sites and LLSVP edges, which is under debate (Austermann et al., 2014; Davies et al., 2015; Doubrovine et al., 2016; Torsvik et al., 2006, 2010), provides important information about how the LLSVPs change their location and shape and the time scale of these changes (Zhong and Liu, 2016).

In the isochemical model, all plumes form on the CMB and strong plumes seem to occur evenly away from subducting regions (Fig. 6b). The preferential occurrence of LIPs near LLSVP margins thus suggests that the LLSVPs are compositionally distinct from their surroundings, which is similar to that found by Hassan et al. (2015).

4.3. Deep mantle plumes beneath Iceland

It is under debate whether the Iceland is caused by deep mantle plumes from the lowermost mantle (e.g., He et al., 2015), or by upper mantle process such as a broad upwelling bump in the upper mantle (Anderson and Natland, 2014). In the seismic tomography by Montelli et al. (2004), strong seismic velocity reduction beneath Iceland only exists in the upper mantle and they suggested that Iceland may not be caused by mantle plumes from the lower mantle. However, He et al. (2015) provide seismic evidence for a thermochemical plume in the lowermost mantle. Previous geodynamic modeling studies have shown plumes forming in the lowermost mantle beneath Iceland at present-day (Steinberger and Torsvik, 2012; Barnett-Moore et al., 2016). In this context, a number of studies have made attempts in connecting geographic locations of plumes from convection models to the eruption sites of the LIPs (e.g., Steinberger and Torsvik, 2012; Hassan et al., 2015). However, based on our models with different model parameters including Ra and thermodynamic parameters, we find that the precise source locations and timing of most mantle plumes are rather model-dependent and cannot be consistently predicted for all the models. This suggests that although the plate motion history plays a role in organizing large-scale convection in the lower mantle, mantle plume formation is largely controlled by the TBL instability that is sensitive to local and regional details of the TBL and mantle flow. Therefore, caution needs to be exercised in relating mantle plumes from this type of convection models directly to the LIPs.

However, it is worthwhile to point out that all our models with very different parameters show strong mantle plumes forming in the lowermost mantle at locations close to that beneath Iceland, although the precise locations of these plumes vary case by case (Fig. 4a, b and Supplementary Fig. S2). The formation of strong plumes beneath Iceland may be the result of locally converging mantle flows in the lowermost mantle at the north end of the Africa LLSVP (Figs. 1a, 3, and 7a). However, the details of the Iceland volcanism, such as its timing, lateral motion, related surface topography, and volume of melt produced in our models are rather model-dependent due to the nature of TBL instability.

5. Conclusion

In this study, we performed 3D spherical thermochemical and isochemical convection calculations with plate motion history to investigate how parameters including mantle viscosity η, thermal expansivity α and thermal diffusivity κ control the locations of mantle plume formation on the CMB and their relation to the seismically observed LLSVPs. The geodynamic modeling results are compared with theoretical analysis of plume source location, which improves our understanding on the formation of mantle plumes in the lowermost mantle.

We find that although the lower mantle structure is significantly affected by surface plate motion history, the plume formation at the CMB outside of the piles is largely controlled by the instability of thermal boundary layer (TBL). This is supported by a constancy of local Rayleigh number Ra_l (i.e., in the range of 20–40) for all the models that is consistent with critical Rayleigh number Ra_c from marginally stability analysis. We propose a critical distance concept to help understand the plume formation outside the piles in our models. Whether a mantle plume forms outside of the thermochemical piles (i.e., LLSVPs) depends on the critical distance within which the TBL grows thick enough to become unstable and produce mantle plumes. The shorter the critical distance, the more plumes will form outside of the piles. Models with a decrease in α and increase in κ from the surface to the CMB, which are consistent with mineral physics studies, generate a smaller number of mantle plumes forming outside of the piles. High mantle viscosity also significantly suppresses the formation of plumes outside of the piles.

We find much more plumes forming above the middle and at/near the edges of thermochemical piles, which is explained by our theory on plume source location. The strong plumes are preferentially located at/near the edges of thermochemical piles. These plumes may be at least partially derived from materials that have been heated on the CMB outside of the piles and are hotter than that on top of the piles. However, it is possible for some strong plumes that are originated at/near pile edges to later appear above the middle of piles due to lateral movement of plumes and piles and the changes of piles' morphology. ∼65–70% strong plumes are found within 10 degrees from pile edges in our models. For the isochemical model, strong plumes tend to be evenly distributed in the regions away from mantle downwellings. A preferential distribution of the LIPs near the edges of LLSVPs is more consistent with a compositional origin of LLSVPs. All our models show strong mantle plumes beneath Iceland from the lowermost mantle, which supports the deep mantle plume origin of the Iceland volcanism.

Acknowledgements

We would like to acknowledge high-performance computing support from Yellowstone (ark:/85065/d7wd3xhc) provided by NCAR's Computational and Information Systems Laboratory, sponsored by the National Science Foundation. This work is supported by National Science Foundation through grants 1135382 and 1645245.

Appendix A. Supplementary material

Supplementary material related to this article can be found online at http://dx.doi.org/10.1016/j.epsl.2017.08.033.

References

Anderson, D.L., Natland, J.H., 2014. Mantle updrafts and mechanisms of oceanic volcanism. Proc. Natl. Acad. Sci. USA 111, 4298–4304. http://dx.doi.org/10.1073/pnas.1410229111.

Austermann, J., Kaye, B.T., Mitrovica, J.X., Huybers, P., 2014. A statistical analysis of the correlation between large igneous provinces and lower mantle seismic structure. Geophys. J. Int. 197, 1–9. http://dx.doi.org/10.1093/gji/ggt500.

Barnett-Moore, N., Hassan, R., Flament, N., Müller, R.D., 2016. The deep Earth origin of the Iceland plume and its effects on regional surface uplift and subsidence. Solid Earth Discuss., 1–35. http://dx.doi.org/10.5194/se-2016-118.

Bull, A.L., McNamara, A.K., Ritsema, J., 2009. Synthetic tomography of plume clusters and thermochemical piles. Earth Planet. Sci. Lett. 278, 152–162. http://dx.doi.org/10.1016/j.epsl.2008.11.018.

Campbell, I.H., Griffiths, R.W., 1992. The changing nature of mantle hotspots through time – implications for the chemical evolution of the mantle. J. Geol. 100, 497–523.

Courtillot, V., Davaille, A., Besse, J., Stock, J., 2003. Three distinct types of hotspots in the Earth's mantle. Earth Planet. Sci. Lett. 205, 295–308. http://dx.doi.org/10.1016/S0012-821x(02)01048-8.

Davies, D.R., Goes, S., Davies, J.H., Schuberth, B.S.A., Bunge, H.P., Ritsema, J., 2012. Reconciling dynamic and seismic models of Earth's lower mantle: the dominant role of thermal heterogeneity. Earth Planet. Sci. Lett. 353, 253–269. http://dx.doi.org/10.1016/j.epsl.2012.08.016.

Davies, D.R., Goes, S., Sambridge, M., 2015. On the relationship between volcanic hotspot locations, the reconstructed eruption sites of large igneous provinces and deep mantle seismic structure. Earth Planet. Sci. Lett. 411, 121–130. http://dx.doi.org/10.1016/j.epsl.2014.11.052.

Doubrovine, P.V., Steinberger, B., Torsvik, T.H., 2016. A failure to reject: testing the correlation between large igneous provinces and deep mantle structures with EDF statistics. Geochem. Geophys. Geosyst. 17, 1130–1163. http://dx.doi.org/10.1002/2015gc006044.

Dziewonski, A.M., Lekic, V., Romanowicz, B.A., 2010. Mantle Anchor structure: an argument for bottom up tectonics. Earth Planet. Sci. Lett. 299, 69–79. http://dx.doi.org/10.1016/j.epsl.2010.08.013.

Farnetani, C.G., 1997. Excess temperature of mantle plumes: the role of chemical stratification across D″. Geophys. Res. Lett. 24, 1583–1586. http://dx.doi.org/10.1029/97gl01548.

Hager, B.H., Clayton, R.W., Richards, M.A., Comer, R.P., Dziewonski, A.M., 1985. Lower mantle heterogeneity, dynamic topography and the geoid. Nature 313, 541–545.

Hassan, R., Flament, N., Gurnis, M., Bower, D.J., Müller, D., 2015. Provenance of plumes in global convection models. Geochem. Geophys. Geosyst., 1465–1489. http://dx.doi.org/10.1002/2015gc005751.

He, Y.M., Wen, L.X., Capdeville, Y., Zhao, L., 2015. Seismic evidence for an Iceland thermo-chemical plume in the Earth's lowermost mantle. Earth Planet. Sci. Lett. 417, 19–27. http://dx.doi.org/10.1016/j.epsl.2015.02.028.

Hofmann, A.W., 1997. Mantle geochemistry: the message from oceanic volcanism. Nature 385, 219–229. http://dx.doi.org/10.1038/385219a0.

Hofmeister, A.M., 1999. Mantle values of thermal conductivity and the geotherm from phonon lifetimes. Science 283, 1699–1706. http://dx.doi.org/10.1126/science.283.5408.1699.

Howard, L.N., 1966. Convection at high Rayleigh number. In: Görtler, H. (Ed.), Applied Mechanics: Proceedings of the Eleventh International Congress of Applied Mechanics, Munich (Germany), 1964. Springer, Berlin, Heidelberg, pp. 1109–1115.

Ishii, M., Tromp, J., 1999. Normal-mode and free-air gravity constraints on lateral variations in velocity and density of Earth's mantle. Science 285, 1231–1236. http://dx.doi.org/10.1126/science.285.5431.1231.

Jaupart, C., Molnar, P., Cottrell, E., 2007. Instability of a chemically dense layer heated from below and overlain by a deep less viscous fluid. J. Fluid Mech. 572, 433. http://dx.doi.org/10.1017/s0022112006003521.

Labrosse, S., 2002. Hotspots, mantle plumes and core heat loss. Earth Planet. Sci. Lett. 199 (1–2), 147–156. http://dx.doi.org/10.1016/S0012-821X(02)00537-X.

Leng, W., Zhong, S., 2008. Controls on plume heat flux and plume excess temperature. J. Geophys. Res. 113, B04408. http://dx.doi.org/10.1029/2007jb005155.

Li, M., Black, B., Zhong, S., Manga, M., Rudolph, M.L., Olson, P., 2016. Quantifying melt production and degassing rate at mid-ocean ridges from global mantle convection models with plate motion history. Geochem. Geophys. Geosyst. 17, 2884–2904. http://dx.doi.org/10.1002/2016gc006439.

Li, M., McNamara, A.K., Garnero, E.J., 2014. Chemical complexity of hotspots caused by cycling oceanic crust through mantle reservoirs. Nat. Geosci. 7, 366–370. http://dx.doi.org/10.1038/Ngeo2120.

Liu, X., Zhong, S., 2013. Analyses of marginal stability, heat transfer and boundary layer properties for thermal convection in a compressible fluid with infinite Prandtl number. Geophys. J. Int. 194 (1), 125–144. http://dx.doi.org/10.1093/gji/ggt117.

McNamara, A.K., Zhong, S., 2005. Thermochemical structures beneath Africa and the Pacific Ocean. Nature 437, 1136–1139. http://dx.doi.org/10.1038/nature04066.

Montelli, R., Nolet, G., Dahlen, F.A., Masters, G., Engdahl, E.R., Hung, S.-H., 2004. Finite-frequency tomography reveals a variety of plumes in the mantle. Science 303, 338–343. http://dx.doi.org/10.1126/science.1092485.

Moresi, L.N., Solomatov, V.S., 1995. Numerical investigation of 2d convection with extremely large viscosity variations. Phys. Fluids 7 (9), 2154–2162. http://dx.doi.org/10.1063/1.868465.

Morgan, W.J., 1971. Convection plumes in the lower mantle. Nature 230, 42–43. http://dx.doi.org/10.1038/230042a0.

Ni, S., Tan, E., Gurnis, M., Helmberger, D., 2002. Sharp sides to the African superplume. Science 296, 1850–1852. http://dx.doi.org/10.1126/science.1070698.

Olson, P., 1993. Hot spots, swells and mantle plumes. In: Ryan, M.P. (Ed.), Magma Transport and Storage. John Wiley, New York.

Schubert, G., Masters, G., Olson, P., Tackley, P., 2004. Superplumes or plume clusters? Phys. Earth Planet. Inter. 146, 147–162. http://dx.doi.org/10.1016/j.pepi.2003.09.025.

Schuberth, B.S.A., Bunge, H.P., Ritsema, J., 2009. Tomographic filtering of high-resolution mantle circulation models: can seismic heterogeneity be explained by temperature alone? Geochem. Geophys. Geosyst. 10, Q05W03. http://dx.doi.org/10.1029/2009gc002401.

Seton, M., Müller, R.D., Zahirovic, S., Gaina, C., Torsvik, T., Shephard, G., Talsma, A., Gurnis, M., Turner, M., Maus, S., Chandler, M., 2012. Global continental and ocean basin reconstructions since 200 Ma. Earth-Sci. Rev. 113, 212–270. http://dx.doi.org/10.1016/j.earscirev.2012.03.002.

Steinberger, B., Torsvik, T.H., 2012. A geodynamic model of plumes from the margins of Large Low Shear Velocity Provinces. Geochem. Geophys. Geosyst. 13, Q01W09. http://dx.doi.org/10.1029/2011gc003808.

Tackley, P.J., 2002. Strong heterogeneity caused by deep mantle layering. Geochem. Geophys. Geosyst. 3, 1024. http://dx.doi.org/10.1029/2001gc000167.

Tan, E., Leng, W., Zhong, S., Gurnis, M., 2011. On the location of plumes and lateral movement of thermochemical structures with high bulk modulus in the 3-D compressible mantle. Geochem. Geophys. Geosyst. 12, Q07005. http://dx.doi.org/10.1029/2011gc003665.

Torsvik, T.H., Burke, K., Steinberger, B., Webb, S.J., Ashwal, L.D., 2010. Diamonds sampled by plumes from the core-mantle boundary. Nature 466, 352–355. http://dx.doi.org/10.1038/nature09216.

Torsvik, T.H., Smethurst, M.A., Burke, K., Steinberger, B., 2006. Large igneous provinces generated from the margins of the large low-velocity provinces in the deep mantle. Geophys. J. Int. 167, 1447–1460. http://dx.doi.org/10.1111/j.1365-246X.2006.03158.x.

Torsvik, T.H., Steinberger, B., Cocks, L.R.M., Burke, K., 2008. Longitude: linking Earth's ancient surface to its deep interior. Earth Planet. Sci. Lett. 276, 273–282. http://dx.doi.org/10.1016/j.epsl.2008.09.026.

Wen, L., Silver, P., James, D., Kuehnel, R., 2001. Seismic evidence for a thermochemical boundary at the base of the Earth's mantle. Earth Planet. Sci. Lett. 189, 141–153. http://dx.doi.org/10.1016/S0012-821X(01)00365-X.

Whitehead, J.A., 1982. Instabilities of fluid conduits in a flowing Earth – are plates lubricated by the asthenosphere?. Geophys. J. R. Astron. Soc. 70, 415–433.

Williams, C.D., Li, M., McNamara, A.K., Garnero, E.J., van Soest, M.C., 2015. Episodic entrainment of deep primordial mantle material into ocean island basalts. Nat. Commun. 6, 8937. http://dx.doi.org/10.1038/ncomms9937.

Zhang, N., Zhong, S., Leng, W., Li, Z.-X., 2010. A model for the evolution of the Earth's mantle structure since the Early Paleozoic. J. Geophys. Res. 115, B06401. http://dx.doi.org/10.1029/2009jb006896.

Zhong, S., 2005. Dynamics of thermal plumes in three-dimensional isoviscous thermal convection. Geophys. J. Int. 162, 289–300. http://dx.doi.org/10.1111/j.1365-246X.2005.02633.x.

Zhong, S.J., 2006. Constraints on thermochemical convection of the mantle from plume heat flux, plume excess temperature, and upper mantle temperature. J. Geophys. Res., Solid Earth 111, B04409. http://dx.doi.org/10.1029/2005jb003972.

Zhong, S., Liu, X., 2016. The long-wavelength mantle structure and dynamics and implications for large-scale tectonics and volcanism in the Phanerozoic. Gondwana Res. 29, 83–104. http://dx.doi.org/10.1016/j.gr.2015.07.007.

Zhong, S., Zuber, M.T., Moresi, L., Gurnis, M., 2000. Role of temperature-dependent viscosity and surface plates in spherical shell models of mantle convection. J. Geophys. Res. 105, 11063–11082. http://dx.doi.org/10.1029/2000JB900003.

Zhong, S.J., McNamara, A., Tan, E., Moresi, L., Gurnis, M., 2008. A benchmark study on mantle convection in a 3-D spherical shell using CitcomS. Geochem. Geophys. Geosyst. 9, Q10017. http://dx.doi.org/10.1029/2008gc002048.